

# Local control of magnetocrystalline anisotropy in (Ga,Mn)As microdevices: Demonstration in current induced switching

J. Wunderlich,<sup>1</sup> A. C. Irvine,<sup>2</sup> J. Zemen,<sup>3</sup> V. Holý,<sup>4</sup> A. W. Rushforth,<sup>5</sup> E. De Ranieri,<sup>2,1</sup> U. Rana,<sup>2,1</sup> K. Výborný,<sup>3</sup> Jairo Sinova,<sup>6</sup> C. T. Foxon,<sup>5</sup> R. P. Campion,<sup>5</sup> D. A. Williams,<sup>1</sup> B. L. Gallagher,<sup>5</sup> and T. Jungwirth<sup>3,5</sup>

<sup>1</sup>*Hitachi Cambridge Laboratory, Cambridge CB3 0HE, UK*

<sup>2</sup>*Microelectronics Research Centre, Cavendish Laboratory, University of Cambridge, CB3 0HE, UK*

<sup>3</sup>*Institute of Physics ASCR, Cukrovarnická 10, 162 53 Praha 6, Czech Republic*

<sup>4</sup>*Charles University, Faculty of Mathematics and Physics,*

*Department of Electronic Structures, Ke Karlovu 5, 121 16 Prague 2, Czech Republic*

<sup>5</sup>*School of Physics and Astronomy, University of Nottingham, Nottingham NG7 2RD, UK*

<sup>6</sup>*Department of Physics, Texas A&M University, College Station, TX 77843-4242, USA*

(Dated: February 5, 2008)

The large saturation magnetization in conventional dense moment ferromagnets offers flexible means of manipulating the ordered state through demagnetizing shape anisotropy fields but these dipolar fields, in turn, limit the integrability of magnetic elements in information storage devices. We show that in a (Ga,Mn)As dilute moment ferromagnet, with comparatively weaker magnetic dipole interactions, locally tunable magnetocrystalline anisotropy can take the role of the internal field which determines the magnetic configuration. Experiments and theoretical modeling are presented for lithographically patterned microchannels and the phenomenon is attributed to lattice relaxations across the channels. The utility of locally controlled magnetic anisotropies is demonstrated in current induced switching experiments. We report structure sensitive, current induced in-plane magnetization switchings well below the Curie temperature at critical current densities  $\sim 10^5 \text{ Acm}^{-2}$ . The observed phenomenology shows signatures of a contribution from domain-wall spin-transfer-torque effects.

PACS numbers: 75.50.Pp, 75.60.Jk, 85.75.-d

## I. INTRODUCTION

(Ga,Mn)As and related ferromagnetic semiconductors are unique due to their dilute moment nature and the strong spin-orbit coupling.<sup>1,2</sup> Doped with only  $\sim 1$ -10% of Mn magnetic moments, the saturation magnetization,  $M_s$ , and the magnetic dipole interaction fields are  $\sim 100$ -10 times weaker in these materials than in conventional ferromagnets. This could make possible dense integration of ferromagnetic semiconductor microelements with minimal dipolar cross-links. Despite the low  $M_s$  the magnetic anisotropy fields,  $H_a$ , routinely reach  $\sim 10$  mT due to the large, spin-orbit coupling induced magnetocrystalline terms.<sup>3,4</sup> The magnetocrystalline anisotropy can, therefore, take the role normally played by dipolar shape anisotropy fields in the conventional systems. The combination of appreciable and tunable  $H_a$  and low  $M_s$  leads to outstanding micromagnetic characteristics. One particularly important example is the orders of magnitude lower critical current in the spin-transfer-torque magnetization switching<sup>5,6</sup> than observed for dense moment conventional ferromagnets, which follows from the approximate scaling of  $j_c \sim H_a M_s$ . Critical currents for domain wall switching of the order  $10^5 \text{ Acm}^{-2}$  have been reported and the effect thoroughly explored in perpendicularly magnetized (Ga,Mn)As thin film devices at temperatures close to the Curie temperature.<sup>7,8,9</sup>

Here we demonstrate that it is possible to locally tune and control spin-orbit coupling induced magnetocrystalline anisotropies in (Ga,Mn)As, which is achieved

in our devices by lithographically producing strain relaxation. This is the central result of our work and it represents the necessary prerequisite for future highly integrated microdevices fabricated in the dilute-moment ferromagnets. It also makes possible a range of new studies of extraordinary magnetotransport and magnetization dynamics effects in such systems. As a demonstration we link the achieved local control of magnetocrystalline anisotropy with a study of current induced domain wall switching which is currently one of the most hotly debated areas of theoretical and experimental spintronics research.<sup>7,8,9,10,11,12,13,14,15,16,17,18,19,20,21,22,23,24,25</sup> We report in-plane domain-wall switchings well below the Curie temperature at  $j_c \sim 10^5 \text{ Acm}^{-2}$  whose characteristics strongly depend on the locally induced changes of magnetic anisotropy. The phenomenology of the current induced switching we observe shows signatures of domain wall spin-transfer-torque effects.

The paper is organized as follows: In Section II A we introduce the studied (Ga,Mn)As microstructures and the anisotropic magnetoresistance (AMR) technique for detecting local magnetization orientation along the channels.<sup>19</sup> This technique is particularly useful in dilute moment ferromagnets where direct imaging methods, such as the magneto-optical Kerr effect, lack the required sensitivity due to the low  $M_s$ . Numerical simulations of the lattice relaxation in the microbars and microscopic calculations of the corresponding changes of magnetocrystalline anisotropies are discussed in Section II B. Current induced switching experiments in our structures

with locally controlled anisotropies are presented in Section III. A brief summary of the main results is given in Section IV.

## II. LATTICE RELAXATION AND LOCAL CONTROL OF MAGNETIC ANISOTROPY

### A. Experiment

Fig. 1 shows scanning electron micrographs of one of the devices studied. The structure consists of a macroscopic Van der Pauw device and an L-shaped channel patterned on the same wafer, the arms of which are Hall-bars aligned along the  $[1\bar{1}0]$  and  $[110]$  directions. The trench-isolation patterning was done by e-beam lithography and reactive ion etching in a 25 nm thick  $\text{Ga}_{0.95}\text{Mn}_{0.05}\text{As}$  epilayer, which was grown along the  $[001]$  crystal axis on a GaAs substrate. Results for two samples are reported: device A(B) has  $4(1) \mu\text{m}$  wide,  $80(20) \mu\text{m}$  long Hall bars. Isolated magnetic elements with the dimensions of these Hall bars and  $M_s \sim 50 \text{ mT}$  of the  $\text{Ga}_{0.95}\text{Mn}_{0.05}\text{As}$  would have in-plane shape anisotropy fields below  $\sim 1 \text{ mT}$ , which is an order of magnitude lower than the magnetocrystalline anisotropy fields. In-plane shape anisotropies are further reduced in our devices as they are defined by narrow (200nm) trenches with the remaining magnetic epilayer left in place. The Curie temperature of 100 K was obtained from Arrot plots of anomalous Hall data. Hole density of  $5 \times 10^{20} \text{ cm}^{-3}$  was estimated from high-field Hall measurements. At this doping the compressive strain in the  $\text{Ga}_{0.95}\text{Mn}_{0.05}\text{As}$  epilayer grown on the GaAs substrate produces a strong magnetocrystalline anisotropy which forces the magnetization vector to align parallel with the plane of the magnetic epilayer.<sup>3,4</sup>

Magnetization orientations in the individual microbars are monitored locally by measuring longitudinal and transverse components of the AMR at in-plane magnetic fields. The magnetization rotation experiments at saturation magnetic field measured on device B and on the macroscopic Van der Pauw device are presented in Figs. 2(a) and (b). (For the detailed discussion of the origins of the AMR and microscopic modeling of this extraordinary magnetoresistance coefficient in (Ga,Mn)As see Ref. 26.) Examples of magnetoresistance measurements for external magnetic field sweeps in which the field angle  $\theta$ , measured from the  $[1\bar{1}0]$  axis, is constant are shown in Figs. 2(c) and (d). The strongly  $\theta$ -dependent low-field magnetoresistance is attributed to magnetization rotations. At high fields, the magnetoresistance becomes purely isotropic, i.e., the differences between resistances for different angles  $\theta$  become independent of the magnitude of the external field. This property and the much smaller magnitude of the isotropic magnetoresistance compared to the low-field anisotropic magnetoresistance allows us to use the high-field measurements in Figs. 2(a),(b) for determining the one to one correspon-

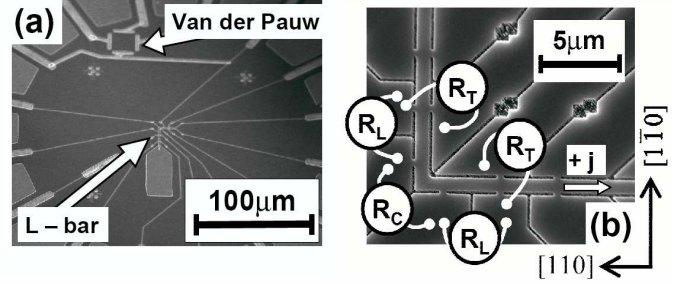


FIG. 1: (a) Scanning electron micrograph of the L-shaped microdevice B and the macroscopic Van der Pauw device. (b) Detail of the L-shaped microdevice with the longitudinal (L) and transverse (T) resistance contacts in the bars and the corner (C) resistance contacts. Positive hole current in the p-type (Ga,Mn)As is defined to propagate from the  $[1\bar{1}0]$ -bar to the  $[110]$ -bar.

dence between a change in the low-field resistance and a change in magnetization orientation. Note that the  $45^\circ$  phase shift between the longitudinal and transverse AMR traces (see Figs. 2(a),(b)) allows us to determine unambiguously the change in the magnetization angle if both resistance components are measured simultaneously. The technique of detecting magnetization rotations via AMR measurements is exploited in Section III where we compare field induced and current induced magnetization switchings. Importantly, the multiterminal design of our L-shaped microbars also allows to apply this electrical measurement of magnetization angle locally at the corner and at different parts of the L-shaped Hall bars and, therefore, to track the propagation of domain walls if present in the system.

In this section we use the fixed- $\theta$  magnetoresistance measurements to first determine local magnetic anisotropies in the individual microbars. Values of  $\theta$  corresponding to easy-axis directions have the smallest low-field magnetoresistance. For values of  $\theta$  not corresponding to easy-axis directions the magnetization undergoes a (partially) continuous rotation at low fields resulting in different orientations, and hence different measured resistances, at saturation and remanence. We find that the technique can be used to determine the easy-axis directions within  $\pm 1^\circ$ .

The effect of microfabrication on the magnetic anisotropy is apparent in Fig. 3. In the bulk, magnetization angle  $30^\circ$  corresponds to an easy-axis while  $7^\circ$  and  $55^\circ$  are significantly harder. For device B,  $7^\circ$  is an easy-axis in the  $[1\bar{1}0]$ -bar and  $55^\circ$  is an easy-axis in the  $[110]$ -bar. All easy-axes found in devices A and B and in the bulk are summarized in Tab.I. The bulk material has the cubic anisotropy of the underlying zincblende structure plus an additional uniaxial  $[1\bar{1}0]$  anisotropy as is typical (Ga,Mn)As epilayers.<sup>27</sup> This results in two easy-axes tilted by  $15^\circ$  from the  $[100]$  and  $[010]$  cube edges towards

the  $[1\bar{1}0]$  direction. In the microdevices, the easy-axes are rotated from their bulk positions towards the direction of the respective bar and the effect increases with decreasing bar width.

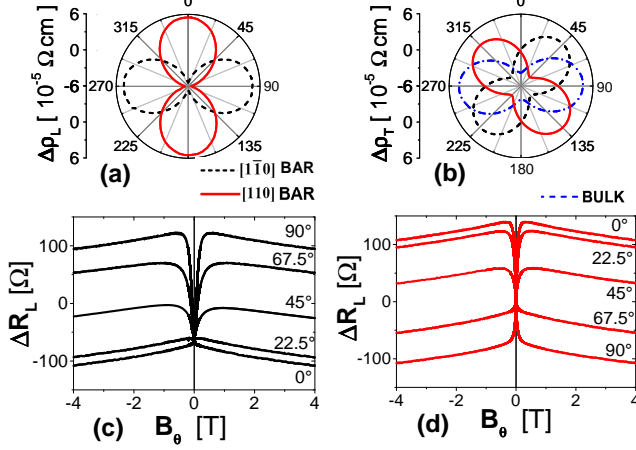


FIG. 2: Device B longitudinal (a) and transverse (b) AMRs measured at 4.2 K in a rotating 4 T in-plane field with the field angle measured from the  $[1\bar{1}0]$  axis, and bulk transverse AMR measured in the Van der Pauw device with current lines oriented along the  $[010]$  axis. ( $\Delta\rho \equiv \rho - \bar{\rho}$  where  $\bar{\rho}$  is the average value over all angles.) In-plane, fixed-angle field sweep measurements of the longitudinal magnetoresistances of the (c)  $[1\bar{1}0]$ -bar and (d)  $[110]$ -bar bar of device B. (Same average resistances as in (a) and (b) are subtracted to obtain  $\Delta R$ )

sample	bulk	A $[1\bar{1}0]$	A $[110]$	B $[1\bar{1}0]$	B $[110]$
easy-axis angle	$\pm 30^\circ$	$\pm 15^\circ$	$\pm 36^\circ$	$+7^\circ, -8^\circ$	$+55^\circ, -63^\circ$

TABLE I: Easy-axes angles, measured from the  $[1\bar{1}0]$  crystal direction, determined by magnetoresistance measurements in the macroscopic Van der Pauw device (bulk) and in the  $[1\bar{1}0]$  and  $[110]$ -bars of the L-shaped devices A and B.

## B. Theory

The local changes in the magnetocrystalline anisotropy can be understood in the following way.  $\text{Ga}_{0.95}\text{Mn}_{0.05}\text{As}$  epilayers grown on GaAs substrate are compressively strained in the (001) plane with the typical value of the strain parameter  $f \equiv (a_{\text{GaMnAs}}^* - a_{\text{GaAs}}^*)/a_{\text{GaAs}}^* \approx 0.2 - 0.3\%$ , where  $a_{\text{GaAs}}^*$  and  $a_{\text{GaMnAs}}^*$  are the lattice parameters of the cubic fully relaxed GaAs and (Ga,Mn)As film, respectively. With the (Ga,Mn)As material removed in the trenches along the bars, the lattice can relax in the transverse direction and the corresponding extension can be roughly estimated as  $ft/w \sim 0.01\%$ ,

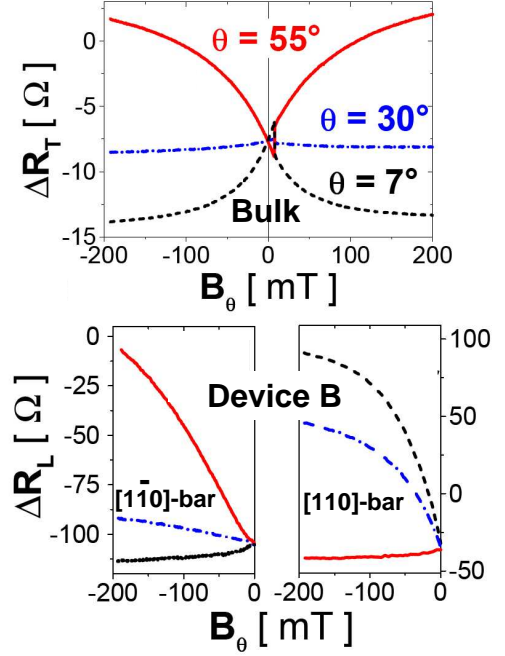


FIG. 3: Comparison of the low-field measurements at 4.2 K of the transverse resistance in the bulk Van de Pauw device (upper panel) and of the longitudinal resistance of the  $[1\bar{1}0]$  and  $[110]$ -bar in device B (lower panels).

where  $t = 25$  nm is the thickness of the (Ga,Mn)As film and  $w$  is the bar width.

On a quantitative level, the strength of the lattice relaxation in the microbars is obtained from numerical elastic theory simulations for the realistic sample geometry. (GaAs values of the elastic constants are considered for the whole wafer including the  $\text{Ga}_{0.95}\text{Mn}_{0.05}\text{As}$  epilayer.) Results of such calculations are illustrated in Fig. 4 for the  $[1\bar{1}0]$ -bar of device B. In panel (a) we show the strain component along the growth-direction  $[001]$ -axis with respect to the lattice parameter of a fully relaxed cubic GaAs,  $e_{[001]} = (a_{[001]} - a_{\text{GaAs}}^*)/a_{\text{GaAs}}^*$ . Since all strain components scale linearly with  $f$  we plot  $e_{[001]}/f$ . The figure highlights the growth induced lattice matching strain; because of the in-plane compression of the (Ga,Mn)As lattice the elastic medium reacts by expanding the lattice parameter in the growth direction, as compared to  $a_{\text{GaMnAs}}^*$ , i.e.,  $e_{[001]}/f > 1$ .

Within the plane, the lattice can relax only in the direction perpendicular to the microbar orientation. The corresponding strain component, calculated again with respect to the GaAs, is plotted in Fig. 4(b) over the entire cross-section of device B and, in Figs. 4(c) and (d), along various cuts through the  $[001]$ - $[110]$  plane. While in the center of the bar the in-plane relaxation is relatively weak, i.e. the lattice parameter remains similar to that of the GaAs substrate, the lattice is strongly relaxed near the edges of the bar. Averaged over the entire cross-

section of the (Ga,Mn)As bar we obtain relative in-plane lattice relaxation of several hundredths of a per cent, i.e., of the same order as estimated by the  $ft/w$  expression. The microscopic magnetocrystalline energy calculations discussed in the following paragraphs confirm that these seemingly small lattice distortions can fully account for the observed easy-axis rotations in the strongly spin-orbit coupled (Ga,Mn)As.

Our microscopic calculations of the magnetization angle dependent total energies are based on combining the six-band  $\mathbf{k} \cdot \mathbf{p}$  description of the GaAs host valence band with kinetic-exchange model of the coupling to the local  $\text{Mn}_{\text{Ga}}$   $d^5$ -moments.<sup>3,4</sup> The theory is well suited for the description of spin-orbit coupling phenomena in the top of the valence band whose spectral composition and related symmetries are dominated, as in the familiar GaAs host, by the  $p$ -orbitals of the As sublattice. The  $\mathbf{k} \cdot \mathbf{p}$  modeling also provides straightforward means of accounting for the effects of lattice strains on the (Ga,Mn)As band structure.<sup>3,4</sup> (As in the above macroscopic simulations we assume that the elastic constants in (Ga,Mn)As have the same values as in GaAs.) This theory, which uses no adjustable free parameters, describes accurately the sign and magnitude of the AMR data in Fig. 2.<sup>26</sup> It has also explained the previously observed transitions between in-plane and out-of-plane easy magnetization orientations in similar (Ga,Mn)As epilayers grown under compressive and tensile strains and provided a consistent account of the signs and magnitudes of corresponding AMR effects.<sup>2</sup>

For the modeling of the magnetocrystalline energy of the microbars we assume homogeneous strain in the (Ga,Mn)As layer corresponding to the average value of  $e_{[110]}$  obtained in the macroscopic elastic theory simulations. The input parameters of the microscopic calculations<sup>3,4</sup> are then strain components, related to the fully relaxed cubic (Ga,Mn)As lattice, in the [100]-[010]-[001] ( $x-y-z$ ) coordinate system which are given by:

$$e_{ij} = \begin{pmatrix} e_{xx} & e_{xy} & 0 \\ e_{yx} & e_{yy} & 0 \\ 0 & 0 & e_{zz} \end{pmatrix} = \begin{pmatrix} \frac{e_{[110]} - f}{2} & \pm \frac{e_{[110]}}{2} & 0 \\ \pm \frac{e_{[110]}}{2} & \frac{e_{[110]} - f}{2} & 0 \\ 0 & 0 & e_{[001]} - f \end{pmatrix}, \quad (1)$$

where  $\pm$  corresponds to the  $[1\bar{1}0]$ -bar and  $[110]$ -bar respectively.

In Fig. 5(b) we plot calculated magnetocrystalline energies as a function of the in-plane magnetization angle for  $f = 0.3\%$  and  $e_{xy}$  ranging from zero (no in-plane lattice relaxation) to typical values expected for the  $[1\bar{1}0]$ -bar ( $e_{xy} > 0$ ) and for the  $[110]$ -bar ( $e_{xy} < 0$ ). Consistent with the experiment, the minima at [100] and [010] for  $e_{xy} = 0$  move towards the  $[1\bar{1}0]$  direction for lattice expansion along [110] direction ( $e_{xy} > 0$ ) and towards the  $[110]$  direction for lattice expansion along  $[1\bar{1}0]$  direction ( $e_{xy} < 0$ ). Note that the asymmetry between experimental easy-axes rotations in the two bars is due to the

a  $[110]$ -uniaxial component present already in the bulk material whose microscopic origin is not known but can be modeled<sup>27</sup> by an intrinsic (not induced by micropatterning) strain  $e_{xy}^{\text{bulk}} \sim +0.01\%$ .

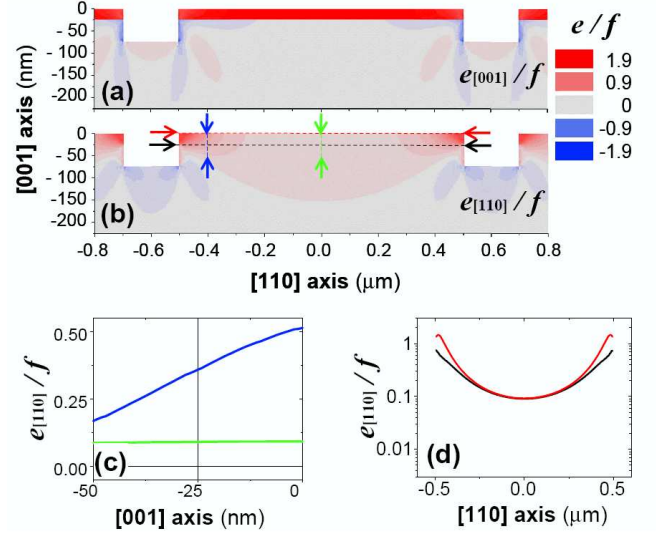


FIG. 4: Numerical simulations of lattice parameters in the  $1 \mu\text{m}$  wide  $[1\bar{1}0]$ -bar of device B defined by  $200 \text{ nm}$  wide and  $75 \text{ nm}$  deep trenches in the  $25 \text{ nm}$  thick (Ga,Mn)As film on a GaAs substrate. (a) Strain component along the [001]-axis with respect to the lattice parameter of a fully relaxed cubic GaAs,  $e_{[001]} = (a_{[001]} - a_{\text{GaAs}}^*)/a_{\text{GaAs}}^*$ . The epitaxial growth induced strain parameter  $f$  is defined as,  $f = (a_{\text{GaMnAs}}^* - a_{\text{GaAs}}^*)/a_{\text{GaAs}}^*$  where  $a_{\text{GaMnAs}}^* > a_{\text{GaAs}}^*$  is the lattice parameter of the cubic fully relaxed (Ga,Mn)As film. (b) Same as (a) for in-plane strain component  $e_{[110]}$  in the direction perpendicular to the bar orientation. (c) and (d) Strain components  $e_{[110]}$  along different cuts through the [001]-[110] plane. The cuts and the corresponding  $e_{[110]}/f$  curves are highlighted by colored arrows in (c) and (d) and the corresponding color coding of curves in (c) and (d).

### III. DEMONSTRATION IN CURRENT INDUCED SWITCHING

The L-shaped geometry of our devices is well suited for a systematic study of the link between the locally adjusted magnetic anisotropies in the individual microbars and their current induced switching characteristics. Apart from the distinct magnetocrystalline anisotropy fields, the two bars in each device have identical material parameters and lithographical dimensions. They can also be expected to share a common domain-wall nucleation center at the corner of the L-shaped channel since in this region the lattice relaxation effects and the corresponding enhancement of the magnetocrystalline anisotropies are less pronounced. Apart from this effect, the domain wall nucleation at the corner can be expected to be sup-



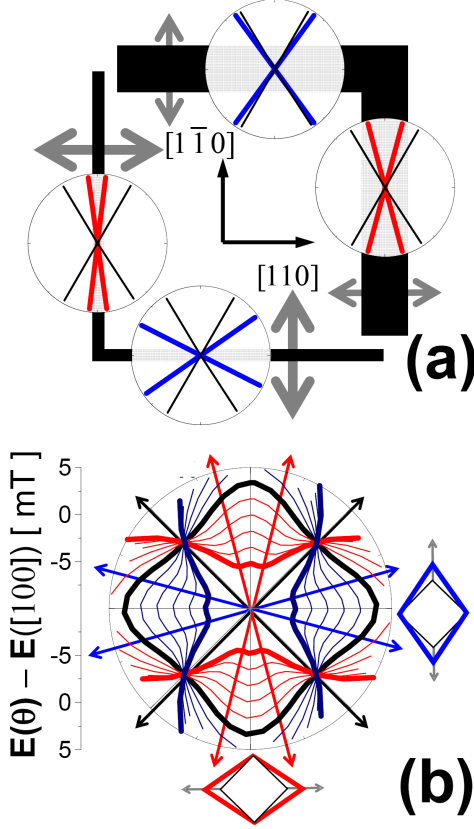


FIG. 5: (a) Schematics of the easy-axes orientations in the  $[1\bar{1}0]$  and  $[110]$ -bars of the L-shaped devices A and B. Arrows indicate the direction and strength of the patterning induced lattice relaxation. (b) Theoretical magnetocrystalline energies as a function of the in-plane magnetization angle for zero shear strain (black line), for  $e_{xy} = 0.004, \dots, 0.02\%$  (red lines) corresponding to lattice extension along  $[110]$  axis, and for  $e_{xy} = -0.004, \dots, -0.02\%$  (blue lines) corresponding to lattice extension along  $[1\bar{1}0]$  axis. The magnetic easy-axes at  $e_{xy} = 0, 0.02\%$  and  $-0.02\%$  are highlighted by black, red, and blue arrows, resp. Lattice deformations breaking the  $[1\bar{1}0]$ - $[110]$  symmetry of the microscopic magnetocrystalline energy profile are illustrated by the diamond-like unit cells extended along  $[110]$  axis for the  $[1\bar{1}0]$ -bar (red diamond) and along the  $[1\bar{1}0]$  axis for the  $[110]$ -bar (blue diamond).

ported by an enhanced current induced heating in this part of the device.

The basic phenomenology of current induced switchings that we observe in all our L-shaped microbars is illustrated in Figs. 6 and 7. The particular field-assisted switching data plotted in the figures were measured in the  $[110]$ -bar of device A at  $\theta = 7^\circ$ . At this off-easy-axis angle the current induced switching can be easily induced and detected due to the hysteretic bistable character of the low field magnetization and the clear AMR signal upon reversal (see Fig. 7(a)). We start with assessing the role of heating in the current induced switching experiments. Figs. 6(a) and (b) compare the temperature dependence of the longitudinal resistance at low

current density ( $10^3 \text{ Acm}^{-2}$ ) with the dependence on current density measured in liquid helium. As seen from the plots, the maximum current density of  $1 \times 10^6 \text{ Acm}^{-2}$  used in the experiments corresponds to heating the sample by approximately 20 K, which is well below the Curie temperature of 100 K. Nevertheless, a suppression due to heating of the effective barrier between metastable and stable states and thermally induced reversals are possible near the switching fields and these effects have to be considered when analyzing the current induced switching experiments below.

The measurements presented in Figs. 7(b)-(f) were performed by first applying a saturation field and then reversing the field and setting it to a value close to but below the switching field in the field-sweep experiment (see Fig. 7(a)). Then, the first current ramp was applied which triggered the reversal, followed by subsequent control current ramps of the same polarity which showed no further changes in the magnetization. Constant current sweep rate of  $5 \times 10^4 \text{ Acm}^{-2}\text{s}^{-1}$  was used in all experiments. In Figs. 7(b)-(f) we plot the difference,  $\delta R$ , between resistances of the first and the subsequent current ramps. We note that no switchings were observed in these experiments up to the highest applied currents in the  $[1\bar{1}0]$ -bar. In this bar with the stronger magnetocrystalline anisotropy, the magnitude of the low current ( $10^3 \text{ Acm}^{-2}$ ) switching field at  $\theta = 7^\circ$  is  $\approx 8 \text{ mT}$ , as compared to the  $\approx 5.5 \text{ mT}$  switching field in the  $[110]$ -bar.

First we discuss data in Fig. 7(b) and (c) taken at  $-4 \text{ mT}$  external field and negative current ramps. The two independent experiments (panels (b) and (c) respectively) performed at nominally identical conditions demonstrate the high degree of reproducibility achieved in our devices. This includes the step-like features which we associate with domain wall depinning/pinning events preceding full reversal. To understand this process in more detail we complement the longitudinal (black curve) and transverse (red curve) resistance measurements in the  $[110]$ -bar with the resistance measurements at the corner (blue curve) of the L-shaped channel. The schematic plot of the respective voltage probes is shown in the inset. The first magnetization switching event at  $j \approx -5 \times 10^5 \text{ Acm}^{-2}$  is detected by the step in the  $\delta R_C$  signal, i.e., occurs in the corner region between the  $R_C$  contacts. For current densities in the range between  $j \approx -5 \times 10^5 \text{ Acm}^{-2}$  and  $j \approx -6 \times 10^5 \text{ Acm}^{-2}$  the domain wall remains pinned in the corner region. The next domain wall propagation and pinning event in  $\delta R_C$  is observed between  $j \approx -6 \times 10^5 \text{ Acm}^{-2}$  and  $j \approx -7 \times 10^5 \text{ Acm}^{-2}$  and for  $|j| > 7 \times 10^5 \text{ Acm}^{-2}$  the region between the  $R_C$  contacts is completely reversed. The depinning events at  $j \approx -5 \times 10^5 \text{ Acm}^{-2}$  and  $j \approx -6 \times 10^5 \text{ Acm}^{-2}$  are also registered by the  $R_L$  and  $R_T$  contacts through noise spikes in the respective  $\delta R_L$  and  $\delta R_T$  signals. However, beyond these spikes,  $\delta R_L$  and  $\delta R_T$  remain constant for  $|j| < 7 \times 10^5 \text{ Acm}^{-2}$  indicating that the domain wall has not reached the section of the  $[110]$ -bar between the  $R_L$  contacts at these current densities. Constant  $\delta R_C$  and

step-like changes in  $\delta R_L$  and  $\delta R_T$  at  $|j| > 7 \times 10^5 \text{ Acm}^{-2}$  are signatures of the domain wall leaving the corner section and entering the part of the  $[110]$ -bar between the  $R_L$  contacts. The reversal of this part is completed at  $j \approx -8 \times 10^5 \text{ Acm}^{-2}$ . Note that both the  $\delta R_L$ , averaging over the whole bar between the longitudinal contacts, and the  $\delta R_T$ , reflecting the local structure near the respective transverse contacts, show switching at the same current and the sense and magnitude of the overall change in  $\delta R_L$  and  $\delta R_T$  are consistent with those observed in the field sweep measurement (see Fig. 7(a)). This indicates that the contacts have a negligible effect on the anisotropy in this bar and allows us to unambiguously determine the magnetization angles of the initial state,  $39 \pm 1^\circ$ , and of the final state,  $211 \pm 1^\circ$ . This -4 mT field assisted current induced switching is not observed at positive current ramps up to the highest experimental current density of  $j = 1 \times 10^6 \text{ Acm}^{-2}$  which indicates that spin-transfer-torque effects can be contributing to the reversal. Note also that the domain wall propagates in the direction opposite to the applied hole current, in agreement with previous spin-transfer-torque studies of perpendicularly magnetized (Ga,Mn)As films.<sup>8</sup> (The anomalous direction of the domain wall propagation is assigned to the anti-ferromagnetic alignment of hole spins with respect to the total moment in (Ga,Mn)As.<sup>7,8,9</sup>)

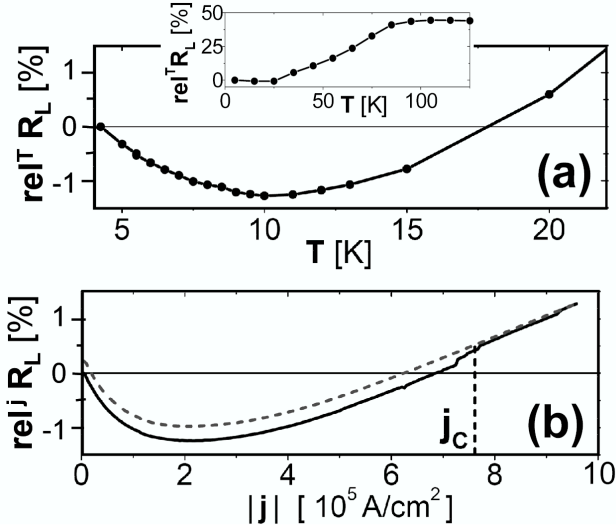


FIG. 6: (a) Temperature dependence of  $\text{rel}^T R_L \equiv [R_L(T) - R_L(4.2)]/R_L(4.2)$  at current density  $10^3 \text{ Acm}^{-2}$ . For completeness,  $\text{rel}^T R_L$  over a wide range of temperatures below and above the Curie temperature is shown in the inset. (b) First (solid line) and second (dashed line) current ramps at -4 mT field applied along  $\theta = 7^\circ$ ; relative resistances are plotted with respect to the zero-current resistance in the first ramp. Switching at  $j_c \approx -7.5 \times 10^5 \text{ Acm}^{-2}$  is marked.

A suppression of the role of the spin-transfer-torque relative to the thermally assisted switching mechanism

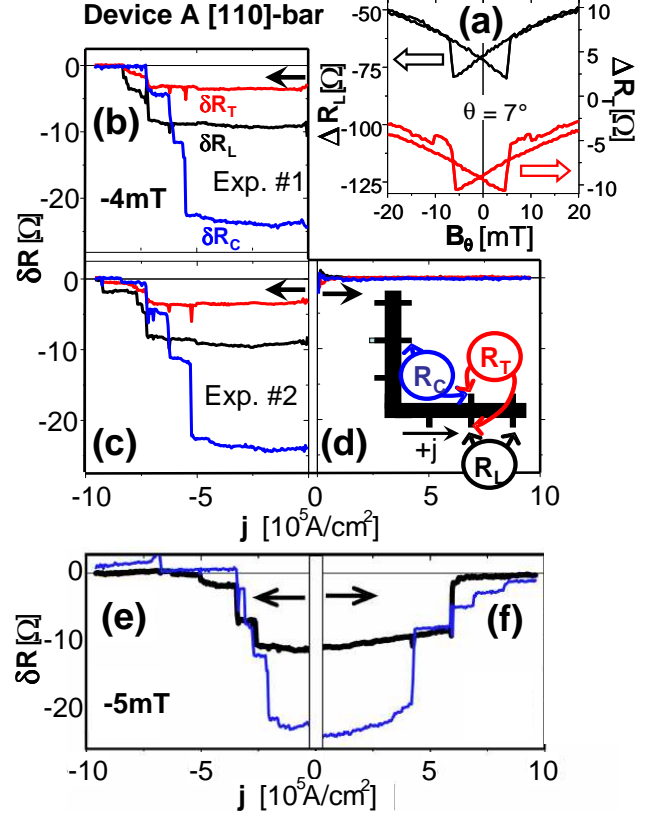


FIG. 7: (a) Field-sweep measurements at  $\theta = 7^\circ$  in the  $[110]$ -bar of device A. (b) Differences between the first and second negative current ramps for the longitudinal (black lines) and transverse (red lines) resistance in the  $[110]$ -bar and in the corner (blue lines) of device A at -4 mT external field applied along  $\theta = 7^\circ$ . Arrows indicate the current ramp direction. (c) Same as (b) for the second independent experiment. (d) Same as (b) and (c) for positive current ramps. The inset shows contacts used for measurements of  $R_L$ ,  $R_T$ , and  $R_C$  in all panels. (e), (f) -5 mT field assisted current induced switching experiments.

is expected at fields closer to the coercive field. The data taken at -5 mT field shown in Fig. 7(e) and (f) are fully consistent with this expectation. Current induced switchings are observed here at lower critical currents and for both current polarities. Nevertheless, the asymmetry between the negative and positive critical currents is still apparent and consistent with a picture of cooperative effects of heating and spin-transfer-torque for negative currents and competing effects of the two mechanisms for positive currents.

The distinct current induced switching characteristics achieved by patterning one bar along the  $[110]$  direction and the other bar along the  $[1\bar{1}0]$  direction are illustrated in Figs. 8 and 9 on a set of experiments in device B. The measurements shown in Figs. 8(b)-(d) were taken on the

$[1\bar{1}0]$ -bar in an external field of a magnitude of -9 mT applied along  $\theta = 0^\circ$  (see corresponding field sweep measurements in Fig. 8(a)). Up to the highest experimental current densities, the switching (from magnetization angle  $9^\circ$  to  $180^\circ$ ) is observed only for the positive current polarity. A less detailed tracking of the domain wall is possible in this experiment compared to the data in Fig. 7 due to the larger magnitude of the external field (larger coercive field of device B) and smaller separation of the contacts used to monitor  $R_C$  in this device. Nevertheless, the -9 mT field assisted reversal process shown in Fig. 8 is clearly initiated in the corner and, again, the domain wall propagates in the direction opposite to the applied hole current. Since for the opposite magnetic field sweep we observe the current induced switching at +9 mT also at positive currents (compare Figs. 8(b) and (d)), the Oersted fields are unlikely to be the dominant switching mechanism. Note also that the Oersted fields generated by our experimental currents are estimated to be two orders of magnitude weaker than the anisotropy fields.<sup>9</sup>

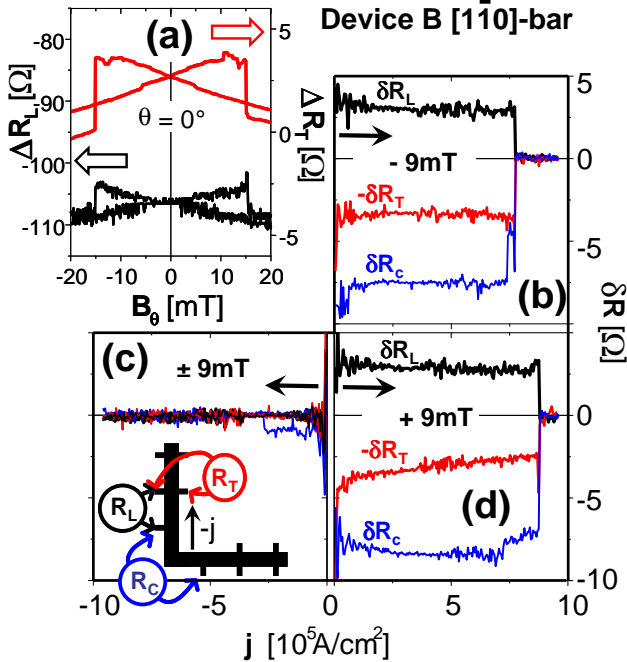


FIG. 8: (a) Field-sweep measurements at  $\theta = 0^\circ$  in the  $[1\bar{1}0]$ -bar of device B. (b) Difference between the first and second positive current ramps in the  $[1\bar{1}0]$ -bar of device B at -9 mT field applied along  $\theta = 0^\circ$ . Note that  $-\delta R_T$  is plotted for clarity. (c) Same as (b) at negative current ramps at  $\pm 9$  mT. The inset shows contacts used for measurements of  $R_L$  and  $R_T$  in all panels. (d) Same as (b) at +9 mT field.

The character of the current induced switching in device B at -9 mT is completely different in the  $[110]$ -bar compared to the  $[1\bar{1}0]$ -bar, as shown in Figs. 9(c) and

(d). The switching occurs at much lower current densities due to the lower coercive field of the  $[110]$ -bar at  $\theta = 0^\circ$  (compare Figs. 8(a) and 9(a)), and the asymmetry between the positive and negative switching currents is small, suggesting that heating plays an important role in this experiment. Although we see clear jumps in  $\delta R_L$ , which are consistent with the field-sweep data in Fig. 9(a), the absence of the  $\delta R_T$  switching signal in the  $[110]$ -bar hinders the unambiguous determination of the switching angles. This feature is ascribed to a fabrication induced strong pinning at the  $R_T$  contacts; indeed the field-sweep measurements for the  $[110]$ -bar show an incomplete switching at 10 mT in the longitudinal resistance and no clear signature of switching for the transverse resistance contacts at this field. (Full saturation of the entire bar including the transverse contacts region is achieved at 100 mT.)

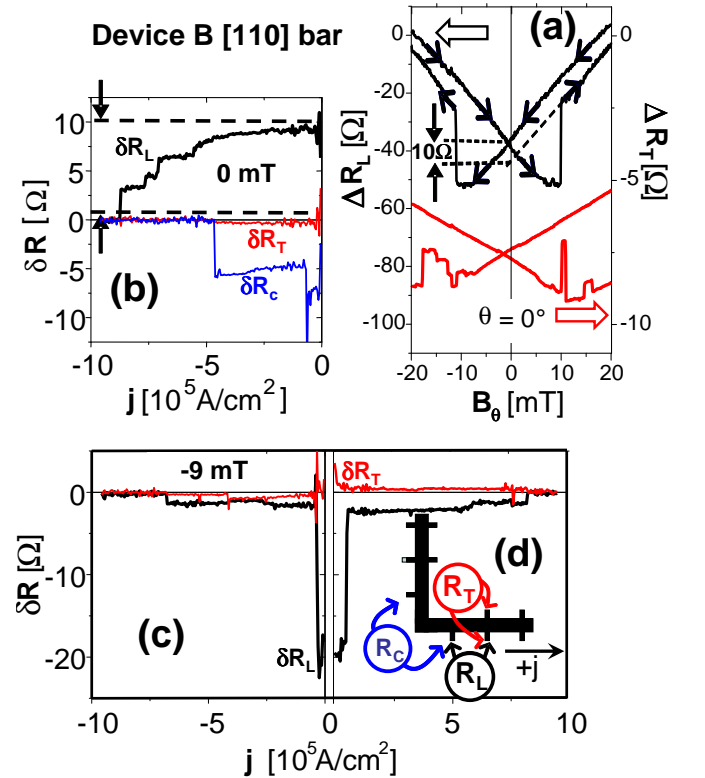


FIG. 9: (a) Field-sweep measurements at  $\theta = 0^\circ$  in the  $[110]$ -bar of device B. (b) Difference between the first and second negative current ramps in the  $[110]$ -bar of device B at zero field. (c) Difference between the first and second negative current ramps at -9 mT field applied along  $\theta = 0^\circ$ . (d) Same as (c) at for positive current ramps. The inset shows contacts used for measurements of  $R_L$  and  $R_T$  in all panels.

In Fig. 9(b) we exploit the pinning at the  $R_T$  contacts to study current induced switching at zero magnetic field. Note that if the switching of the whole bar was complete the zero-field  $180^\circ$  rotation from negative to positive easy-axis directions would be undetectable by the

AMR measurement. We again see no switching signal in  $\delta R_T$  but a clear step in  $\delta R_L$ . As for all field-assisted experiments, the sense and magnitude of the jump in  $\delta R_L$  for zero field correlates well with the field sweep measurements (see the dashed line in Fig. 9(a)). Also consistent with the trends in the field-assisted experiments, the switching occurs at larger current than in the -9 mT field assisted switching. Up to the highest experimental current density, the zero-field switching is observed only in the negative current ramp, as we would expect for the domain wall propagation from the corner (see the  $\delta R_c$  signal in Fig. 9(b)) to the [110]-bar due to spin-transfer-torque. We emphasize however that a detailed understanding of the origin of the observed current induced switchings in our L-shaped devices is beyond the scope of this work. Our main aim was to demonstrate that the local control of the magnetocrystalline anisotropy we achieved in these dilute moment ferromagnetic structures is a new powerful tool for investigating spin dynamics phenomena.

#### IV. SUMMARY

In summary, (Ga,Mn)As microchannels with locally controlled magnetocrystalline anisotropies and inherently weak dipolar fields represent a new favorable class of systems for exploring magneto-electronic effects at microscale. We have observed easy-axes rotations which depend on the width and crystal orientation of the microchannel. Based on numerical simulations of strain distribution for the experimental geometry and microscopic calculations of the corresponding spin-orbit coupled band structures we have explained the effect in terms of lattice relaxation induced changes in the magnetocrystalline anisotropy. The observation and explanation of micropatterning controlled magnetocrystalline

anisotropy of the (Ga,Mn)As dilute moment ferromagnet represents the central result of our paper. In addition to that we have demonstrated that the structures are well suited for a systematic study of current induced switching phenomena well below Curie temperature at relatively low current densities. We have found indications that domain-wall spin-transfer-torque effects contribute strongly to the observed switchings. This suggests that our structures represent a new favorable system for exploring these technologically important yet still physically controversial spin dynamics phenomena.

*Note added:* After the completion of our work, independent and simultaneous studies of the lattice relaxation induced changes of magnetocrystalline anisotropies in (Ga,Mn)As have been posted on the Los Alamos Archives and some of them published during the processing of our manuscript.<sup>28,29,30</sup> The crystal orientations and widths of the nanochannels considered in these works are different than in our study. Nevertheless, the reported effects are of the same origin and our works provide a mutual confirmation that the seemingly tiny changes in the lattice constant can completely overwrite the magnetocrystalline energy landscape of the host (Ga,Mn)As epilayer.

#### Acknowledgment

We acknowledge discussions with A. H. MacDonald, V. Novák, and support from EU Grant IST-015728, from EPSRC Grant GR/S81407/01, from GACR and AVCR Grants 202/05/0575, 202/06/0025, 202/04/1519, FON/06/E002, AV0Z1010052, LC510, from MSM Grant 0021620834, from NSF Grant DMR-0547875, and from ONR Grant N000140610122.

- 
- <sup>1</sup> F. Matsukura, H. Ohno, and T. Dietl, in *Handbook of Magnetic Materials*, edited by K. H. J. Buschow (Elsevier, Amsterdam, 2002), vol. 14, p. 1, From Ohno Lab Homepage.
  - <sup>2</sup> T. Jungwirth, J. Sinova, J. Mašek, J. Kučera, and A. H. MacDonald, *Rev. Mod. Phys.* **78**, 809 (2006), cond-mat/0603380.
  - <sup>3</sup> T. Dietl, H. Ohno, and F. Matsukura, *Phys. Rev.* **B 63**, 195205 (2001), cond-mat/0007190.
  - <sup>4</sup> M. Abolfath, T. Jungwirth, J. Brum, and A. H. MacDonald, *Phys. Rev.* **B 63**, 054418 (2001), cond-mat/0006093.
  - <sup>5</sup> J. Sinova, T. Jungwirth, X. Liu, Y. Sasaki, J. K. Furdyna, W. A. Atkinson, and A. H. MacDonald, *Phys. Rev.* **B 69**, 085209 (2004), cond-mat/0308386.
  - <sup>6</sup> D. Chiba, Y. Sato, T. Kita, F. Matsukura, and H. Ohno, *Phys. Rev. Lett.* **93**, 216602 (2004), cond-mat/0403500.
  - <sup>7</sup> M. Yamanouchi, D. Chiba, F. Matsukura, and H. Ohno, *Nature* **428**, 539 (2004).
  - <sup>8</sup> D. Chiba, M. Yamanouchi, F. Matsukura, T. Dietl, and H. Ohno, *Phys. Rev. Lett.* **96**, 096602 (2006), cond-mat/0601464.
  - <sup>9</sup> M. Yamanouchi, D. Chiba, F. Matsukura, T. Dietl, and H. Ohno, *Phys. Rev. Lett.* **96**, 096601 (2006), cond-mat/0601515.
  - <sup>10</sup> P. P. Freitas and L. Berger, *J. Appl. Phys.* **57**, 1266 (1985).
  - <sup>11</sup> A. Yamaguchi, T. Ono, S. Nasu, K. Miyake, K. Mibu, and T. Shinjo, *Phys. Rev. Lett.* **92**, 077205 (2004).
  - <sup>12</sup> E. Saitoh, H. Miyajima, T. Yamaoka, and G. Tatara, *Nature* **432**, 203 (2004).
  - <sup>13</sup> G. Tatara and H. Kohno, *Phys. Rev. Lett.* **92**, 086601 (2004), cond-mat/0308464.
  - <sup>14</sup> Z. Li and S. Zhang, *Phys. Rev.* **B 70**, 024417 (2004).
  - <sup>15</sup> G. Tatara, N. Vernier, and J. Ferre, *Appl. Phys. Lett.* **86**, 252509 (2004), cond-mat/0411250.
  - <sup>16</sup> S. E. Barnes and S. Maekawa, *Phys. Rev. Lett.* **95**, 107204 (2005).
  - <sup>17</sup> A. Thiaville, Y. Nakatani, J. Miltat, and Y. Suzuki, *Europhys. Lett.* **69**, 990 (2005).
  - <sup>18</sup> G. Gould, K. Pappert, C. Rüster, R. Giraud, T. Borzenko, C. M. Schott, K. Brunner, G. Schmidt, and L. W. Molenkamp, *Jpn. J. Appl. Phys.* **1 45**, 3860 (2006), cond-



- mat/0602135.
- <sup>19</sup> M. Hayashi, L. Thomas, Y. B. Bazaliy, C. Rettner, R. Moriya, X. Jiang, and S. S. P. Parkin, Phys. Rev. Lett. **96**, 197207 (2006).
  - <sup>20</sup> L. Thomas, M. Hayashi, X. Jiang, R. Moriya, C. Rettner, and S. S. P. Parkin, Nature **443**, 197 (2006).
  - <sup>21</sup> V. K. Dugaev, V. R. Vieira, P. D. Sacramento, J. Barnas, M. A. N. Araújo, and J. Berakdar, Phys. Rev. **B 74**, 054403 (2006).
  - <sup>22</sup> J. Xiao, A. Zangwill, and M. D. Stiles, Phys. Rev. **B 73**, 054428 (2006).
  - <sup>23</sup> J. I. Ohe and B. Kramer, Phys. Rev. Lett. **96**, 027204 (2006).
  - <sup>24</sup> M. A. N. Araújo, V. K. Dugaev, V. R. Vieira, J. Berakdar, and J. Barnas, Phys. Rev. **B 74**, 224429 (2006), cond-mat/0610235.
  - <sup>25</sup> R. A. Duine, A. S. Núñez, and A. H. MacDonald, Phys. Rev. Lett. **98**, 056605 (2007), cond-mat/0607663.
  - <sup>26</sup> A. W. Rushforth, K. Výborný, C. S. King, K. W. Edmonds, R. P. Campion, C. T. Foxon, J. Wunderlich, A. C. Irvine, P. Vašek, V. Novák, et al. (2007), cond-mat/0702357.
  - <sup>27</sup> M. Sawicki, K.-Y. Wang, K. W. Edmonds, R. P. Campion, C. R. Staddon, N. R. S. Farley, C. T. Foxon, E. Papis, E. Kaminska, A. Piotrowska, et al., Phys. Rev. **B 71**, 121302 (2005), cond-mat/0410544.
  - <sup>28</sup> S. Hümpfner, M. Sawicki, K. Pappert, J. Wenisch, K. Brunner, C. Gould, G. Schmidt, T. Dietl, and L. W. Molenkamp, Appl. Phys. Lett. **90**, 102102 (2007), cond-mat/0612439.
  - <sup>29</sup> K. Pappert, S. Hümpfner, C. Gould, J. Wenisch, K. Brunner, G. Schmidt, and L. W. Molenkamp (2007), cond-mat/0701478.
  - <sup>30</sup> J. Wenisch, C. Gould, L. Ebel, J. Storz, K. Pappert, M. J. Schmidt, C. Kumpf, G. Schmidt, K. Brunner, and L. W. Molenkamp (2007), cond-mat/0701479.